# Stereotypical spatiotemporal activity patterns during slow-wave activity in the neocortex

**Thomas Fucke, Dymphie Suchanek, Martin P. Nawrot, Yamina Seamari, Detlef H. Heck, Ad Aertsen and Clemens Boucsein**

*J Neurophysiol* 106:3035-3044, 2011. First published 17 August 2011; doi:10.1152/jn.00811.2010

*J Neurophysiol* 106: 3035–3044, 2011.
First published August 17, 2011; doi:10.1152/jn.00811.2010.

# Stereotypical spatiotemporal activity patterns during slow-wave activity in the neocortex

**Thomas Fucke,[1] Dymphie Suchanek,[1] Martin P. Nawrot,[2] Yamina Seamari,[3] Detlef H. Heck,[4] Ad Aertsen,[1,5] and Clemens Boucsein[1,5]**

[1]*Neurobiology and Biophysics, Faculty of Biology, and* [5]*Bernstein Center Freiburg, University of Freiburg, Freiburg, Germany;* [2]*Institute of Biology, Freie Universität Berlin, Berlin, Germany;* [3]*Department of Physiology, University of Malaga, Malaga, Spain;* [4]*Department of Anatomy and Neurobiology, University of Tennessee Health Science Center, Memphis, Tennessee*

Submitted 22 September 2010; accepted in final form 11 August 2011

**Fucke T, Suchanek D, Nawrot MP, Seamari Y, Heck DH, Aertsen A, Boucsein C.** Stereotypical spatiotemporal activity patterns during slow-wave activity in the neocortex. *J Neurophysiol* 106: 3035–3044, 2011. First published August 17, 2011; doi:10.1152/jn.00811.2010.—Alternating epochs of activity and silence are a characteristic feature of neocortical networks during certain sleep cycles and deep states of anesthesia. The mechanism and functional role of these slow oscillations (<1 Hz) have not yet been fully characterized. Experimental and theoretical studies show that slow-wave oscillations can be generated autonomously by neocortical tissue but become more regular through a thalamo-cortical feedback loop. Evidence for a functional role of slow-wave activity comes from EEG recordings in humans during sleep, which show that activity travels as stereotypical waves over the entire brain, thought to play a role in memory consolidation. We used an animal model to investigate activity wave propagation on a smaller scale, namely within the rat somatosensory cortex. Signals from multiple extracellular microelectrodes in combination with one intracellular recording in the anesthetized animal in vivo were utilized to monitor the spreading of activity. We found that activity propagation in most animals showed a clear preferred direction, suggesting that it often originated from a similar location in the cortex. In addition, the breakdown of active states followed a similar pattern with slightly weaker direction preference but a clear correlation to the direction of activity spreading, supporting the notion of a wave-like phenomenon similar to that observed after strong sensory stimulation in sensory areas. Taken together, our findings support the idea that activity waves during slow-wave sleep do not occur spontaneously at random locations within the network, as was suggested previously, but follow preferred synaptic pathways on a small spatial scale.

slow-wave sleep; extracellular electrode array; up/down state; ketamine/xylazine; traveling waves

SPREADING WAVES OF ACTIVITY within neocortical networks are a phenomenon that can be observed under many different conditions. This includes early developmental phases (Katz and Shatz 1996; Wong 1999; Momose-Sato et al. 2007), strong sensory stimulation in various primary sensory areas such as barrel cortex (Ferezou et al. 2006; Petersen et al. 2003), visual cortex (Xu et al. 2007), and motor cortices (Rubino et al. 2006) (for a detailed review see Wu et al. 2008), as well as during slow-wave sleep (Chauvette et al. 2010) and anesthesia-induced slow-wave activity (Steriade et al. 1993a; 1993b; 1993c; Takagaki et al. 2008). This widespread occurrence has led to a strong interest in the mechanisms underlying wave propagation in the neocortex although a functional role of the traveling waves remains unclear. To gain a better understanding of the functional nature of these reoccurring waves during slow-wave sleep, many studies have elucidated important details on the features of the so-called up- and down-states, which are a characteristic of slow-wave activity in single cells and cell populations. In a neocortical network undergoing slow-wave activity, only a certain fraction of the cells within a local volume takes part in action potential firing during the up-state (at least in the superficial layers), as was revealed by calcium imaging studies (Kerr et al. 2005), with a slow drift of the active subpopulation. Multiple parallel intracellular recordings have demonstrated, however, that even the silent cells receive nearly no synaptic input during the down-states, whereas their membrane potential shows strong depolarization and fluctuations during the up-states (Volgushev et al. 2006), demonstrating that the entire network seems to partake in the oscillatory activity (see also Léger et al. 2005). The questions regarding which cells within the network start a new active state and the mechanisms behind its spreading are discussed somewhat controversially: some evidence points toward a thalamic origin (Blethyn et al. 2006; Hughes et al. 2002; Crunelli and Hughes 2010), but, because spontaneous slow-wave activity can also be observed within deafferentiated cortical slabs (Timofeev et al. 2000), it seems that the cortico-thalamic feedback loop might primarily serve to stabilize the oscillations and make them more regular (Steriade et al. 1993b; Timofeev et al. 2000). Recent in vivo studies in cats suggest that, during slow-wave sleep, layer V pyramidal neurons, generally considered the output cells of the local cortical network, seem to activate before those in layer IV, which receive most of the thalamic input (Chauvette et al. 2010). Along these lines, up-state initiation in human subjects seems to be mediated by synaptic input to dendrites located in the supragranular layers, as shown by current source density analysis of layer-specific, local-field-potential recordings. However, in human cortex no leading layer in terms of onset of action potential firing could be identified (Csercsa et al. 2010). Data from acute slice experiments have supported these findings (Sanchez-Vives and McCormick 2000), and the observation that extracellular $Ca^{2+}$ concentrations rapidly increase toward the end of the down-states and gradually decrease during the depolarized up-states (Massimini and Amzica 2001) has also argued in favor of the

Address for reprint requests and other correspondence: C. Boucsein, Neurobiology and Biophysics, Faculty of Biology, Univ. of Freiburg, Schänzlestrasse 1, D-79104 Freiburg, Germany (e-mail: clemens.boucsein@biologie.uni-freiburg.de).

cortical origin hypothesis. Mechanistically, the increased $[Ca^{2+}]_{ext}$ might lead to a cascade of downstream events, including an increase in evoked vesicle release probability (Crochet et al. 2005) and subsequently to a higher frequency of miniature excitatory postsynaptic potentials, which then could ignite a transition into the active state (Chauvette et al. 2010). Theoretical studies, on the other hand, have suggested additional mechanisms that could lead to slow-wave activity starting within the cortical network. If equipped with slightly elevated densities of $I_h$-channels, pyramidal cells might serve as pacemaker cells for a global oscillation (Kang et al. 2008), whereas other theoretical considerations suggest that oscillatory waves could be a generic emergent property of systems with spatially restricted connectivity (Ermentrout and Kleinfeld 2001). Common to all theories is, first, the assumption of a more or less homogeneous distribution of cell types and, second, that oscillatory waves of activity could originate from arbitrary locations within the network.

Because spatiotemporal patterns of traveling waves during slow-wave activity are an experimentally quantifiable phenomenon, we wanted to further characterize the properties of slow-wave activity generation. In particular, we investigated to what extent waves of activity spread through the neocortical network along stereotypical pathways. Studies performed in the anesthetized rat implementing voltage-sensitive dye (VSD) imaging have shown that activity waves have a tendency to propagate along specific paths, even showing cross-modal activation (Takagaki et al. 2008). EEG studies in humans also revealed an origin and preferable direction of wave propagation that was consistent across subjects (Massimini et al. 2004; Riedner et al. 2007). On the other hand, VSD imaging performed in the barrel cortex of awake mice indicated that spontaneous waves varied their direction from one trial to the next (Ferezou et al. 2006). For our study, we implemented a spatially defined array of seven extracellular electrodes in combination with one intracellular electrode and recorded from the somatosensory cortex of rats anesthetized with a combination of urethane and ketamine/xylazine. This kind of anesthesia has been established as a model for slow-wave sleep (Fontanini et al. 2003; Sharma et al. 2010) and leads to stable and regular low-frequency oscillations in the neocortex. Fitting spreading circular waves to our data, we found that wave fronts had a preferred direction of propagation, which varied across animals. This was true for both, activating and inactivating transitions. Our findings suggest that activity waves during slow-wave activity originate from a single location within the network and follow preferred synaptic pathways, which are not predefined by the coarse anatomical structure of the neocortex and may differ across animals.

## MATERIALS AND METHODS

*Animals and surgery.* For the experiments, adult Sprague-Dawley rats (274 to 570 g body wt) were anesthetized with intraperitoneal injections of 20% urethane (1 g/kg body wt), and supplementary doses of a mixture of ketamine and xylazine (100 mg/kg and 5 mg/kg, respectively) were administered every 30–50 min to maintain deep anesthesia as defined by the absence of whisker movements and pinch reflex and the presence of clear state transitions in the intra- and extracellular recordings (see below). Body temperature was measured using a rectal thermometer and maintained between 38–39° C using a heating pad. Although the state transitions also occur under urethane anesthesia alone, the use of ketamine enhances and stabilizes the appearance of up- and down-states. After a deep anesthesia level was achieved, animals were placed into a stereotactic holder, and the skull was exposed. A 1.5 × 1.5 mm bone window was made over the left somatosensory cortex medial to the barrel field (anteroposterior, −2.1 mm; mediolateral, 4.7 mm), and, where necessary, the dura was removed. All experimental procedures used in this study were performed in accordance with the Freiburg University and German guidelines on the use of animals in research.

*Electrophysiological recordings.* For extracellular recordings, an array of glass-coated, single platinum-tungsten microelectrodes was used (0.5 to 0.8 MΩ; Thomas Recording, Giessen, Germany). Seven electrodes were distributed on a 3 × 3 grid with 400 μm interelectrode distance (for *experiments 1–8*; Fig. 1*A, top*). Special care was taken to arrange the tips of the electrodes within the same horizontal plane to ensure recording from the same cortical layer. The dura was removed, and the array was slowly lowered perpendicularly to the pial surface into the brain tissue until clear spikes were detectable on at least five of the seven electrodes. To avoid recordings from subcortical structures, electrodes were never lowered more than 1.5 mm into the tissue. A subset of the experiments (*experiments 9–11*; Fig. 1*A, bottom*) were recorded with an array consisting of seven electrodes distributed on a 3 × 4 grid with an interelectrode distance of 305 μm. Again, the seven electrodes were inserted into the cortical tissue, but this time at an angle of 45° with respect to the pial surface, positioned in such a way as to have a planar arrangement of the electrode tips. This resulted in a distance between the tips of 431 μm in one and 305 μm in the other direction. Here the dura was left intact, and electrodes were lowered independently with the help of microdrives (MiniMatrix system; Thomas Recording) until they reached their final position within the cortex. Signals were preamplified 10× and 19× for the first and second set of recordings, respectively, and then passed through an array of filter amplifiers with a gain of 500 and a bandpass between 100 Hz and 5 kHz (Multi Channel Systems, Reutlingen, Germany).

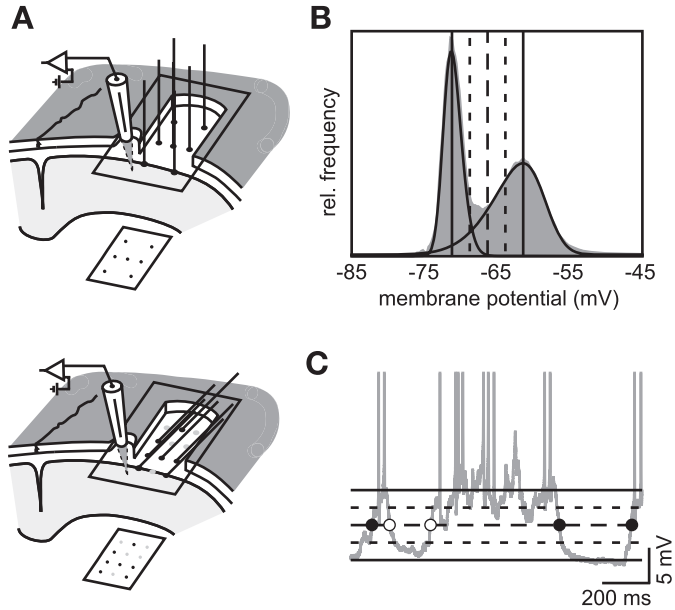


Fig. 1. Recording electrodes layout and transition time detection. *A*: layout of intra- and extracellular electrodes for *experiments 1–8* (*top*) and *9–11* (*bottom*). *B*: voltage histogram (gray) after high-pass filtering of intracellular recording trace. Black curves show the 2 fitted skewed Gaussian functions (*Eq. 1*), the peak values of which are marked by solid vertical lines. Broken lines mark $thresh_{low}$, $thresh_{mid}$, and $thresh_{high}$, respectively (see MATERIALS AND METHODS). *C*: detection of transition times; lines as in *B*. Accepted (●) and rejected (○) transitions are based on silent periods between consecutive down-to-up (DU) and up-to-down (UD) transitions (see MATERIALS AND METHODS).

Simultaneously to the extracellular recordings, one intracellular electrode was placed medially in close vicinity (0.5 to 1 mm) to the electrode array for membrane potential recording of a single cell. For that, microelectrodes with a resistance between 60 and 120 MΩ were pulled from borosilica glass (Hilgenberg, Malsfeld, Germany) on a horizontal Flaming/Brown puller (P97; Sutter Instruments, Novato, CA) and filled with potassium acetate solution (1 M). A total of 11 such combinatorial experiments were recorded. Signals were amplified with a bridge amplifier (SEC05; NPI, Tamm, Germany) and low-pass filtered at 3 kHz. All signals were digitized at 25 kHz (power1401; CED, Cambridge, UK) and stored on a PC for offline analysis.

*Detection of state transitions in intracellular recordings.* In a first step, down-to-up (DU) and up-to-down (UD) state transitions were detected in the voltage traces recorded intracellularly. Low-frequency fluctuations were eliminated by high-pass filtering traces with a second-order Butterworth filter with passband and stopband corner frequencies of 0.5 and 0.2 Hz, respectively. To determine state-transition thresholds, voltage histograms were built over complete filtered traces and fit by a dual skewed normal function (which led to more reliable results than a simple sum of two Gaussians; Fig. 1*B*):

$$n(V) = \sum_i A_i e^{-\frac{(V - V_{0,i})^2}{2\sigma_i^2}} \left(1 + \mathrm{erf}\left(\frac{\alpha_i (V - V_{0,i})}{\sigma_i \sqrt{2}}\right)\right) + B \quad (1)$$

with $i$ = low, high; erf denotes the error function and introduces the skewness parameters $\alpha_i$; $V_{0,i}$, $\sigma_i$, and $A_i$ are the mean, variance and amplitude of the respective distributions; $B$ denotes a global offset. From this fit the two maxima $n_{\mathrm{max,low}}$ and $n_{\mathrm{max,high}}$ and their difference $\Delta n_{\mathrm{max}}$ were determined. We set thresholds to $\mathrm{thresh_{low}} = n_{\mathrm{max,low}} + 0.25\Delta n_{\mathrm{max}}$, $\mathrm{thesh_{mid}} = n_{\mathrm{max,low}} + 0.5\Delta n_{\mathrm{max}}$, and $\mathrm{thresh_{high}} = n_{\mathrm{max,low}} + 0.75\Delta n_{\mathrm{max}}$ (Fig. 1*B*). A state transition was detected in the high-pass filtered intracellular trace if, for DU transitions, voltage passed $\mathrm{thresh_{low}} \rightarrow \mathrm{thresh_{mid}} \rightarrow \mathrm{thresh_{high}}$ or, for UD transitions, $\mathrm{thresh_{high}} \rightarrow \mathrm{thresh_{mid}} \rightarrow \mathrm{thresh_{low}}$ in the respective order; the time point of transition was defined as the time of passing $\mathrm{thresh_{mid}}$. Up- and down-state durations were defined as the time until the next UD or DU transition, respectively. Time points of transitions were accepted for further wave-front analysis if between 50 ms and 200 ms before (after) the DU (UD) transition no voltage value was higher than $\mathrm{thresh_{low}}$ (Fig. 1*C*). We thereby ensured that we could unambiguously detect an approaching wave front in the extracellular recordings. Note that, because of our criteria for accepting transitions, the number of DU transitions ($N_{\mathrm{trans,DU}}$) and UD transitions ($N_{\mathrm{trans,UD}}$) were not the same and that in general there was not necessarily a DU transition (onset of an up-state) for each UD transition (offset of an up-state) for a particular up-state. This discrepancy is not problematic for further analysis steps and does not affect the results reported here.

For determining the distribution of action potentials (APs) after (for UD transitions: before) the transition occurred, we set an AP detection threshold to up state mean voltage plus twice the up state membrane potential standard deviation. Every threshold crossing with a positive flank was then detected as an AP.

*Alignment of signals from extracellular electrodes.* Multiunit activity (MUA) from extracellular recordings was prepared with a root mean square (RMS) procedure (Stark and Abeles 2007). Signals from extracellular electrodes were cut off at twice their standard deviation to reduce the relative weights of units with high amplitudes. Subsequently, traces were squared and low-pass filtered with a fourth-order Butterworth filter with corner and stop frequencies of 100 Hz and 150 Hz, respectively. Finally, the square root of the signal was calculated for further analysis. From the resulting traces, we cut 400-ms windows centered around intracellular state transition times. Data within these windows were then downsampled from 25 kHz to 1 kHz using a fast Fourier transform-based method implemented in the Python-based scientific computing package SciPy (Version 0.5.2; see http://scipy.org/ for details). We thereby ended up with ($N_{\mathrm{trans,DU}} + N_{\mathrm{trans,UD}}$) * $N_{\mathrm{extra\_el}}$ data traces $\lambda(t)$, each containing a state transition, assuming that the traveling wave passed by the respective extracellular electrode. Depending on the spatial spread of the wave, transitions will reach electrodes with different time shifts, which we quantified with respect to the transition time detected in the intracellular recording.

For estimating this temporal shift for each extracellular electrode with respect to the intracellular transition, we used a variant of an algorithm introduced by Nawrot et al. (2003) for optimal temporal realignment of single trial spike responses to a repeated stimulus. For each electrode separately, we chose the first transition as having a shift of $\tau_{1,\mathrm{opt}} = 0$. The remaining $N_{\mathrm{trans}}$-1 shifts ($\tau_{2,\mathrm{opt}} \ \ldots \ \tau_{N,\mathrm{opt}}$) were calculated by first computing the cross-correlograms for each pair ($i$, $j$), $C_{ij}$:

$$C_{ij}(\tau_j - \tau_i) = \int \lambda_i(\tau_i + s)\lambda_j(\tau_j - s)ds \quad (2)$$

Subsequently, a second order polynomial, $p_{ij}(\tau) = a_{ij}\,\tau^2 + b_{ij}\,\tau + c_{ij}$, was fitted to a small window (40 ms) centered around the maximum of each of the $N(N\text{-}1)/2$ correlograms $C_{ij}$. Before correlating, all cut-out MUA traces were multiplied with a window having the value of 1 everywhere, with the exception of the 10-ms border regions, where it decreased as a squared cosine to 0. This procedure forced the maximum of the polynomial into the 400-ms window of the entire correlogram. The sum of all $p_{ij}$, $P(\tau_2 \ldots \tau_N)$, then possesses a unique global maximum that defines the shifts of trials ($2 \ \ldots \ N$) for optimal alignment with the first trial. The time point of an extracellular state transition was then determined as the half-maximum crossing of the mean of the aligned traces. The temporal difference between intra- and extracellular state transition, $\tau_{\mathrm{global}}$, was subsequently subtracted from all single-transition shifts ($\tau_1 \ \ldots \ \tau_N$). Using this procedure, we could estimate the latency of state transitions in extracellular signals relative to intracellular state transitions for each electrode separately. Thus, for each DU and UD transition, we obtained a vector of seven (total number of electrodes used in both our arrays) latencies, which we processed further for measuring the stereotypical nature of the state transitions.

*Fitting of circular wave fronts.* The basic assumption for our analysis was that spontaneous state transitions do not occur simultaneously across the whole cortex but travel as waves through the cortical network (reviewed in Wu et al. 2008). We further assumed that, on the spatial scale of our electrode array, these traveling wave fronts can be well approximated by expanding circular waves. We could thus express the stereotypical nature of reoccurring waves passing the extracellular electrode array on the basis of the angular distribution of the origins of fitted circular wave fronts.

For each transition, we assumed a circular wave that started at origin ($x_0$, $y_0$) at time $t_0$ before it first hit the electrode array and traveled at fixed speed $v$. Then, it will arrive at an electrode $i$ of the array at time:

$$t_i = \frac{1}{v}\sqrt{(x_i - x_0)^2 + (y_i - y_0)^2} - t_0 \quad (3)$$

The four parameters $x_0$, $y_0$, $v$, and $t_0$ were optimized for each transition separately, using a Levenberg-Marquardt algorithm (Press et al. 1992), which is designed to optimize nonlinear functions to a given set of data points. It is implemented in the SciPy package (Version 0.5.2) and based on the sum of squared differences between the experimentally measured latency vector ($\tau_1 \ \ldots \ \tau_7$) and on the vector ($t_1 \ \ldots \ t_7$) based on the circular wave model:

$$\mathrm{Error} = \sum_{i=1}^{7} (\tau_i - t_i)^2 \quad (4)$$

yielding $N_{\mathrm{trans}}$ sets of parameters for each experiment. Thus for each state transition we obtained an estimate for the origin ($x_0$, $y_0$), defining the direction of wave propagation, the speed of the propagating wave front $v$, and time of impact $t_0$.

*Measures of stereotypicity.* Using the parameters computed by circular wave front optimization, we further utilized measures from circular statistics to determine how stereotypically spontaneous state transitions occurred. We were particularly interested in whether origins of circular waves were homogeneously distributed or whether there was a directional preference of wave propagation.

For convenience, we used the central electrode as the origin of a polar coordinate system. Using the origin coordinates, $(x_{0,i}, y_{0,i})$, $i = 1 \ldots N_{\text{trans}}$, one can calculate the set of angles, $\varphi_i$, vs. an arbitrary axis of the coordinate system (in our case the positive $x$-axis of the array, pointing into rostral direction; see Fig. 4*A*). From the distribution of angles, we calculated complex mean vectors as

$$m_1 = \frac{1}{N_{trans}} \sum_i e^{j\varphi_i}$$
$$m_2 = \frac{1}{N_{trans}} \sum_i e^{2j\varphi_i} \quad (5)$$

where $m_1$ and $m_2$ denote the first and second trigonometric moment, respectively. Note that the mean vector strength (the absolute value of $m$) varies between 0 and 1. The circular variance was calculated as (Batschelet 1981)

$$CV = \sqrt{2(1 - |m|)} \quad (6)$$

Additionally, we tested the mean vector strength $|m|$ against its expected value from a purely random distribution of angles with the same $N_{\text{trans}}$. The mean $|m|$ from 1,000 random angular distributions was calculated, as well as its standard deviation. We accepted experimental mean vectors as significant if they were longer than the mean vector strength plus four standard deviations of the simulated uniform distributions.

For testing whether wave front propagation velocities showed a preferred direction, we devised the following test: experimentally, each direction was associated with a velocity. If we permuted the velocities with respect to the directions, any dependencies between the two should be resolved. We performed 1,000 of such permutations and computed the resulting mean angular-velocity (AV) distribution. We then used the mean squared difference as a distance measure to determine which fraction of permuted AV distributions was more different from the mean than the actually observed experimental distribution. This fraction reflects the probability ($P$ value) that the experimental AV distribution derived from the group of permuted AV distributions. A small $P$ value ($P < 0.05$) was then taken as evidence for a nonhomogeneous AV distribution.

## RESULTS

For studying the stereotypical nature of spontaneous state transitions in vivo, simultaneous intra- and extracellular recordings of spontaneous slow-oscillation activity from somatosensory cortex of 11 adult Sprague-Dawley rats were performed. Intracellular recordings lasted between 3 and 12 min. Times of state transitions between down-states and up-states were determined from intracellular recordings and were used to define a search window on the data from the extracellular electrodes, within which the times of state transition for the local cell population sampled by each extracellular electrode were defined. The latency differences between extracellular electrodes were used to fit an expanding circular wave front characterizing the wave of activity traveling over the cortical surface. Subsequently, the parameters from this fit were used to determine how stereotypical the observed state transitions were on a single trial basis.

*Characterization of intracellularly recorded state transitions.* We first wanted to assure that the slow-wave activity observed in our preparation was comparable to that reported in other studies. Spontaneous state transitions in vivo have been observed to occur with a frequency of around 1 Hz and to span a membrane potential range of 10–15 mV (Steriade et al. 1993a; Léger et al. 2005; Volgushev et al. 2006). We confirmed the occurrence of slow oscillations in our intracellular recordings by autocorrelating the intracellular signal (Fig. 2*A*, *left*). The temporal period of the resulting side peaks of the correlogram was 0.97 ± 0.21 s (range 0.76 to 1.40), i.e., mean oscillation frequencies of 1.07 ± 0.20 Hz (Fig. 2*A*, *right*). Membrane potential histograms showed two clearly discernible peaks, which could be fitted well by a sum of two skewed normal functions (*Eq. 1*). Experiments for which the second peak could not be unequivocally identified were excluded from further analysis. The voltage difference between the two peaks was 9.8 ± 2.6 mV and thus within the range of values reported previously. The clear separability of these peaks allowed us to determine state-transition times with high precision in the intracellular recording. Membrane potentials during down-states were −80.3 ± 18.3 mV.

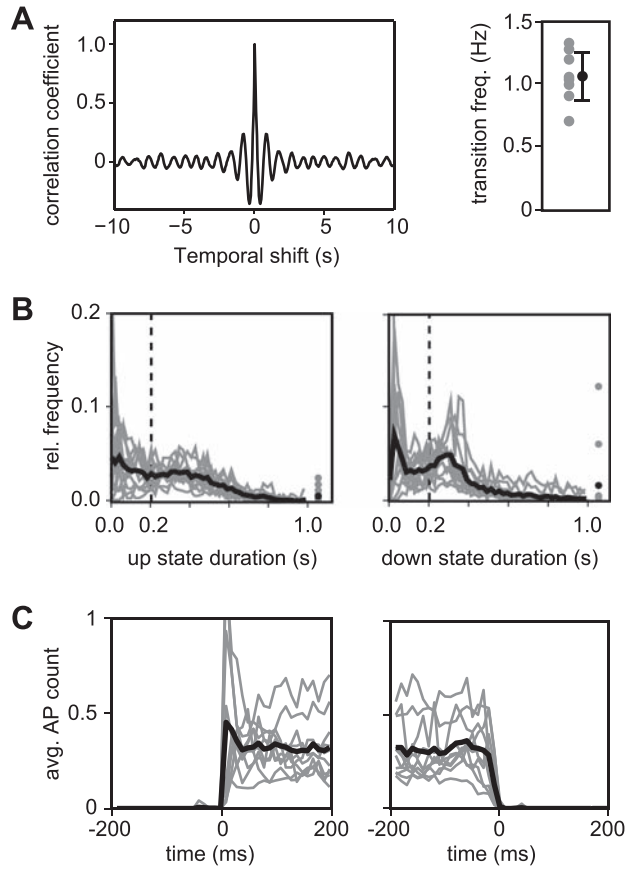


Fig. 2. Characteristics of intracellularly recorded membrane potential fluctuations. *A*, *left*: example autocorrelogram (total time 1 min) of intracellular raw data from single intracellular recording. *Right*: distribution of state-transition frequencies as extracted from autocorrelograms (gray dots: single experiments; black dot: mean across experiments). *B*, *left* and *right*: distribution of the up-state and down-state durations, respectively. Gray traces represent individual experiments, and the black traces indicate the mean overall experiments. The dashed vertical line at 200 ms depicts the minimum state duration used for further analysis (see text). *C*, *left*: normalized action potential (AP) distribution histogram for the DU transition (bin width 20 ms). Gray traces show distributions from individual experiments, and the black trace is the mean over all experiments ($n = 11$). *Right*: same as in *left*, but for the UD transition.

Histograms of up-state and down-state durations (Fig. 2*B*, *left* and *right*) revealed a weakly bimodal distribution, with local minima at around 200 ms and 100 ms in the up- and down-state distributions, respectively. For our analysis of the stereotypical nature of transitions, we could only use state transitions that allowed the reconstruction of wave fronts and, therefore, discarded short-lasting states, where state onsets and offsets were often difficult to assign. In addition, latencies between the intra- and the extracellular transition could reach up to 150 ms (Fig. 3*B*). As a minimum duration, we thus chose the local minimum in the up-state length distribution (200 ms). After the exclusion of state transitions followed by short states, 73.5 ± 4.5% for DU transitions and 76.9 ± 4.1% for UD transitions were used for further analysis. The length of cut-out windows for extracellular data was then set to 400 ms and divided symmetrically around the intracellular state transition, gathering an approximately sigmoidal shape of the extracellular spike-rate profiles within the cut-out window (see Fig. 7 in Léger et al. 2005).

*Temporal shifts between electrodes in the array.* To detect direction and speed of traveling-activity wave fronts, we measured the time differences of wave-front arrival at the different electrodes within the extracellular recording array. In contrast to the detection of state transitions in intracellular recordings, where voltage thresholds allow for an unambiguous definition of the transition time, APs recorded with extracellular electrodes do not necessarily mark state transitions because the first AP can occur with considerable jitter after the membrane

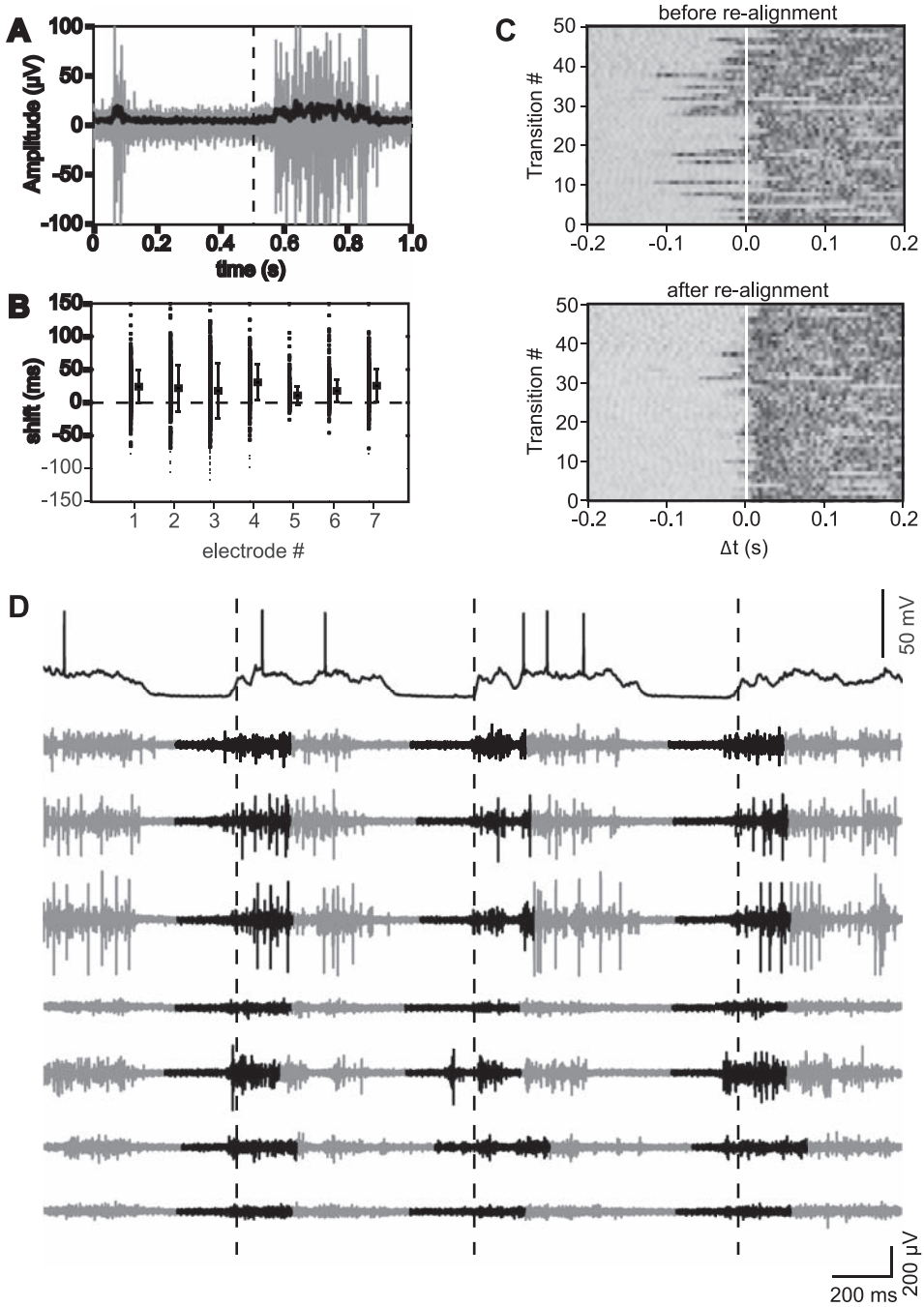


Fig. 3. Extracellular multiunit activity (MUA) data and implementation of realignment algorithm. *A*: example of an extracellular recording, centered on the intracellular state transition (dashed line). The gray trace indicates raw data; the black trace shows data after processing (see MATERIALS AND METHODS). *B*: calculated shifts for a single experiment, showing mean and SD for each extracellular electrode (indicated by dot and bar, respectively) and individual shifts for each transition (gray dots). *C*: 50 filtered extracellular traces (as black trace in *A*), randomly chosen from 1 electrode (during the same experiment), centered around intracellular state transition onset (white line) before (*top*) and after (*bottom*) realignment algorithm was applied. *D*: example of 3 s of intracellular raw data (*top*) and the 7 simultaneously recorded extracellular raw traces (*bottom 7*). Dashed lines indicate intracellular DU transition onset, and the black highlighted MUA signal shows 400-ms windows after realignment shifts were applied (see MATERIALS AND METHODS).

potential has reached the up-state. This problem can be reduced by averaging over a local population of neurons because most cells take part in slow oscillations in a concerted manner (Volgushev et al. 2006; Kerr et al. 2005). Extracellular electrodes with an impedance close to 1 MΩ pick up signals from neurons in a volume of roughly 100-$\mu$m diameter around the electrode tip (Stark and Abeles 2007), which contains between 20 and 30 neurons in the neocortex, assuming a cell density of 90,000 cells per mm$^3$ (Gabbott and Stewart 1987). To get a reasonable estimate of the transition time of the local population, we used a combination of two procedures: in a first step, we applied an RMS procedure (see MATERIALS AND METHODS) to the extracellular signals from each electrode (Fig. 3*A*). This method is advantageous for an unbiased estimation of the activity of a larger population of neurons recorded by a single electrode because high-amplitude APs from cells that are located close to the electrode tip are truncated. This is especially important for the second step in our analysis, the extraction of transition times by applying a realignment algorithm (see MATERIALS AND METHODS), because the measurement of the optimal time shift could otherwise easily be dominated by a few high-amplitude AP units. The realignment algorithm was used because it allows for reliable response detection in noisy single-trial data (see Nawrot et al. 2003). Because with this algorithm the error in shifts based on less steep noisy flanks is bigger, we extracted the histograms of AP occurrences (Fig. 2*C*, *left* and *right*). These histograms should allow us to estimate the sharpness of state transitions in extracellular recordings under the assumption that the firing pattern extracted from the intracellular recording is representative for the cells generating the signals captured by the extracellular electrodes. From the appearance of the histograms, we should expect sharper DU transitions than UD transitions (Léger et al. 2005). This potentially renders the shifts of UD transitions less reliable compared with those of DU transitions. The realignment algorithm itself was used to align single cut-out windows from a given electrode such that the observed signals became maximally similar (Fig. 3*C*). For each transition, the latencies of all electrodes (Fig. 3*B*) relative to the intracellular recording (Fig. 3*D*) were then used for estimating the parameters of a single activity wave front moving across the electrode array.

*Traveling wave fronts of DU transitions.* To assess how stereotypical the state transitions were, we applied circular statistics to the distribution of directions pointing toward the extrapolated origins of circular waves fit to the transition latencies of the extracellular electrodes (Fig. 4*A*). The stereotypical nature was quantified by calculating the mean vector (*Eq. 5*) of the directions for all state transitions in an experiment. The direction of the mean vector indicates the preferred direction; its length (the mean vector strength) is a measure for the relative frequency of its occurrence. The mean vector strength ranges from 0 to 1, corresponding to no and maximally stereotypical behavior, respectively. Three examples of direction distributions of DU transitions are shown in Fig. 4*B* (*top*). The average mean vector strength over all experiments was 0.45 ± 0.25 (range 0.08 to 0.74). These values correspond to an average circular variance (*Eq. 6*) of 59° (range 77.7 to 41.3°), meaning that transitions had a strong bias toward the preferred direction of propagation. To assess the statistical significance of the observed vector strengths, we compared them to the expected values of 1,000 uniformly distributed, random-angle distributions with the same number of transitions each. We considered a mean vector strength as highly significant if it exceeded the simulated mean vector strength by four standard deviations from the control

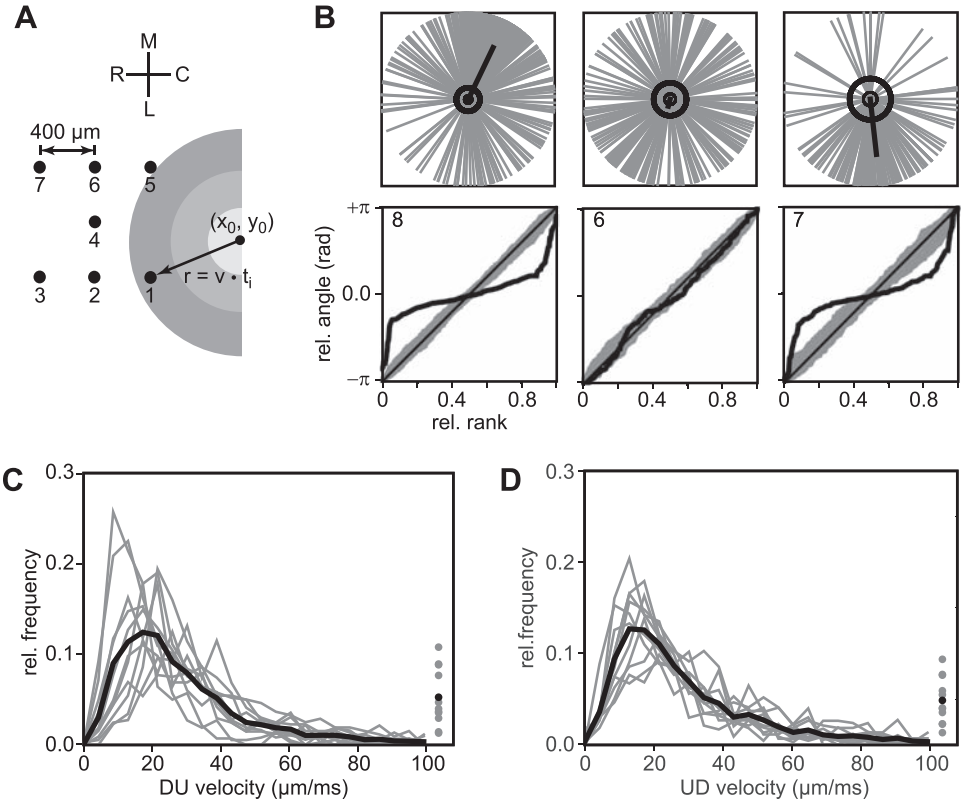


Fig. 4. Circular wave-front analysis of state transitions. *A*: schematic illustration showing circular wave origin ($x_0$, $y_0$) and expanding wave fronts propagating across the multielectrode array. Positions and identities of electrodes are indicated by black dots, labeled accordingly. The interelectrode distance was 400 $\mu$m for the first set and 431 and 305 $\mu$m for the second set of experiments (see MATERIALS AND METHODS). M, medial; L, lateral; C, caudal; R, rostral. *B*: examples of directional distributions (quiver plots, *top*) and resulting rank plots (*bottom*). Mean directions in quiver plots are indicated by thick vectors; mean vector length and 4× SD resulting from 1,000 uniform angular distributions are shown as inner and outer circles, respectively. In the rank plots, thick black lines depict experimental angular distribution. Gray lines show 200 uniform angular distributions, and thin black line is the equidistant distribution. Before generating rank plots, the mean angle was subtracted. Numbers in the upper left-hand corners of the rank plots indicate the experiment number, asterisk indicates significance. *C* and *D*: distributions of wave-front velocities of DU and UD transitions, respectively. Gray traces show distributions from single experiments, and the average across experiments is shown in black. Velocities larger than 100 $\mu$m/ms are pooled into a single bin at the far right of the respective histogram.

surrogate data (inner and outer black circles in Fig. 4*B*, *top*, respectively). This was the case in 10 out of 11 experiments. For a better visualization of deviations of experimentally observed angular distributions from uniformly random distributions, we plotted angles from single transitions against their relative rank within the distribution of angles (Fig. 4*B*, *bottom*). To allow for a better comparison over different experiments, we aligned the mean angles along the positive *x*-axis (angle 0°). This way, experimental data can be easily compared with simulated uniform distributions (gray traces in Fig. 4*B*, *bottom*). This visualization, similar to the reported mean vector lengths, demonstrates that most experiments showed a clear preference for one direction of the wave of activity spreading over the cortical tissue. Using a sliding-window (width: 10 transitions) approach, we examined the temporal evolution of the mean direction. For all experiments, fluctuations around the mean direction stayed well within the circular variance over the recording period (data not shown).

One main concern during our analysis was that, during the experiments, electrodes might not have been aligned in one single plane but could have picked up MUA signals from different layers. It has been described in previous studies that up-states might be initiated in deep layers first (Sanchez-Vives and McCormick 2000; Chauvette et al. 2010; Sakata and Harris 2009; Csercsa et al. 2010). Indeed, additional experiments, where the electrodes of the 3 × 4 electrode array were positioned vertically in three different cortical layers (Supplemental Fig. S1*A*; supplemental material for this article is available online at the *Journal of Neurophysiology* website), in some cases showed temporal lead in deep layers (Supplemental Fig. S1*B*). To test whether one electrode introduces such a systematic error to our wave-front parameter estimation, we performed the same analysis again with one electrode left out in turn. For most experiments, no qualitative changes of our results were observed (Supplemental Fig. S2*A*). For two experiments, however, we found electrodes that, when left out, reduced the significance of our results. We marked these experiments in Fig. 5*A* by asterisks in parentheses.

By comparing the second trigonometric moment ($m_2$; *Eq. 5*) to the first moment ($m_1$) we determined whether the angular distributions were monomodal ($m_1 > m_2$) or bimodal ($m_2 > m_1$). One would expect a bimodal distribution when waves of activity were reflected at a border between areas (Xu et al. 2007) and, hence,

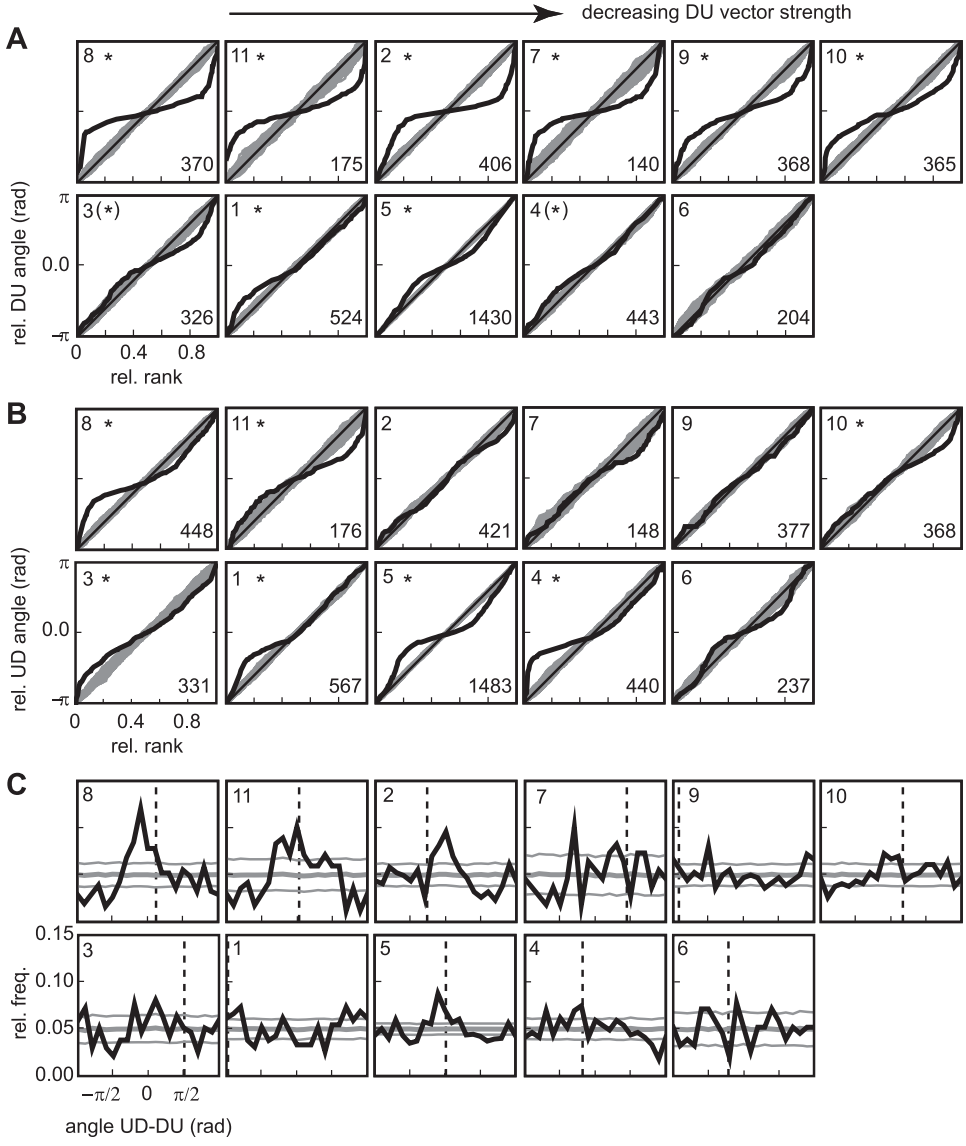


Fig. 5. Analysis of angular distributions of wave-front origins. *A*: angular rank plots of DU transitions of single experiments, sorted by decreasing DU mean vector strength (*Eq. 5*). Format as in *Fig. 4B*. *B*: angular rank plots of UD transitions of single experiments, ordered as in *A*. Format as in *A*. *C*: distributions of angular differences between DU and UD transitions (thick black lines), sorted by decreasing DU mean vector strength. Gray horizontal lines indicate angular difference distribution mean and SD of 1,000 artificial uniformly distributed DU and UD angular distributions with the same number of state transitions each. Dashed vertical lines depict the angle between mean DU and UD vectors. The numbers located in the upper left-hand corners in *A* to *C* indicate the number of the individual experiment. Significance is indicated by asterisks in *A* and *B*, and the number in the lower right corner indicates the number of transitions used for the respective plot.

would pass our electrode array consecutively in opposite directions. For DU transitions, the average $m_2$ vector strength was 0.30 ± 0.14 (range 0.15 to 0.55). The corresponding $m_1$-to-$m_2$ ratio was 1.51 ± 0.64 (>1 in 10 of 11 experiments; the remaining 1 experiment was not significant compared with a uniform random distribution). These findings clearly show that DU transition directions were unimodally distributed.

We next measured the mean median propagation velocity of DU transition wave fronts from the circular wave-front fits, as 25.8 ± 7.6 μm/ms (range: 15.1 to 37.8 μm/ms). Despite this high variability in median velocities, velocity histograms looked similar for all experiments (Fig. 4*C*, gray traces), resulting in a smooth mean velocity distribution across all experiments (Fig. 4*C*, black trace). This distribution shows a distinct peak at 19 μm/ms. A permutation test (see MATERIALS AND METHODS) revealed that, in 4 of 11 experiments, the experimental AV distribution deviated significantly ($P < 0.05$) from a randomized AV distribution in one or more angular bins. However, we could not find a clear correlation between the peaks of the AV distribution and the preferred direction of wave-front origins.

*Traveling wave fronts of UD transitions.* Previous imaging studies suggested that the activity at the end of up-states does not simply die out without a spatiotemporal structure but that, instead, the UD transition travels as a circular wave front similar to that of the DU transition (Xu et al. 2007). To test this in our experimental data, we applied the same analysis as above to UD transitions.

We observed that the distribution of directions toward the origin of the wave front for single experiments (plotted in Fig. 5*B* as rank plots) looks more diffuse than that observed for DU transitions (Fig. 5*A*). The average mean vector strength was 0.30 ± 0.13 (range 0.13 to 0.46), meaning an average circular variance of 68° (range 76° to 60°, respectively). However, with the use of the same test against uniform random angular distributions as for DU transitions, only 7 of 11 experiments showed significantly stereotypical transitions, based on mean vector strength. Again, no dependence of mean direction on experimental time was observed (see above). Also, leaving out one electrode in turn from our analysis (see above) did not change our results.

As for DU transitions, we used the second trigonometric momentum to test bimodality vs. monomodality of the direction distribution. The average vector strength for $m_2$ was 0.24 ± 0.1 (range 0.08 to 0.36). The ratio between $m_1$ and $m_2$ was 1.49 ± 0.92 (range 0.4 to 3.4), again showing a clearly unimodal distribution.

The distribution of velocities (Fig. 4*D*) looked similar to that observed for DU transitions, with an average median velocity of 24.8 ± 5.2 μm/ms (range 18.4 to 33.7 μm/ms). Again, the average of velocity distributions across experiments showed a distinct peak, now at 16 μm/ms. Experimental AV distributions deviated significantly ($P < 0.05$) from randomized AV distributions in 7 of 11 experiments. Again, the relation between AV distribution peaks and preferred direction of wave-front origins remained unclear.

We next asked the question whether DU and UD transitions at the beginning and end, respectively, of the same up-state shared the same properties regarding direction toward wave origin and propagation velocity. Velocities of DU and respective UD wave fronts did not correlate (all $P$ values >0.05, Spearman's rank test). We tested the dependence of UD wave-front direction on DU wave-front direction by computing the distribution of their angular differences, $\Delta\phi$ (Fig. 5*C*). In those experiments, where both DU and UD vector strength were particularly large, a clear peak around $\Delta\phi = 0$ emerged, showing that a large fraction of UD waves traveled in the same direction as the preceding DU wave front.

## DISCUSSION

In the present study, we examined the stereotypical behavior of spontaneous transitions between up- and down-states in the somatosensory cortex of anesthetized rats. We used extracellularly recorded MUA triggered on intracellular state transitions to determine the temporal shifts of wave-front arrivals between different electrodes. This is, to our knowledge, the first study where a large number of such spontaneous DU and UD transitions was used from the same animal to systematically analyze the wave-front propagation during slow-wave activity on a microscopic scale (Massimini et al. 2004; Volgushev et al. 2006). In the vast majority of experiments, we observed a clear, highly significant unimodal distribution of wave-front traveling directions. Results from previous studies regarding stereotypical behavior of state transitions on a cellular level are contradictory: Luczak et al. (2007) reported highly stereotypical activation of single units upon state transitions, independent of wave-front direction. Another study, using optical imaging methods to observe a smaller population of cells, did not find any stereotypical firing behavior of single cells (Kerr et al. 2005). However, the latter experiments covered a much smaller spatial scale, thereby potentially stressing local fluctuations.

The results presented here indicate that activity propagation in most animals showed a clear preferred direction, a behavior that may originate from the repeated early activation of an excitatory pathway often originating from a single location in the cortex (Vyazovskiy et al. 2009). In other words, there seems to be a cortical "hot spot", where up-states are initiated and subsequently travel as clearly defined wave fronts across the cortex. In how far activity at this location is triggered by cortical cells, or by thalamic input, cannot be judged from our data. The same holds true for the underlying physiological mechanism: spontaneous synaptic release, followed by activation of persistent sodium currents (Timofeev et al. 2000; Bazhenov et al. 2002; Chauvette et al. 2010), could cause the observed stereotypical wave generation if one assumes that certain cells have a particularly low threshold to release synaptic vesicles. Similarly, up-states could arise from autonomously oscillating pacemaker cells (Kang et al. 2008) forming the hot spot. It will be interesting to see in future experiments whether in different sleep cycles these hot spots appear at different locations or whether they are preferentially located at a single position in the cortex of the respective individual. Moreover, as we found neither the same directional preference nor a similar origin of the traveling waves across animals, the corresponding difference between presumed hot spots across animals needs to be explained.

*Methodological constraints.* The basic assumption for this study is the circular shape of the traveling wave fronts. This view is supported by voltage-sensitive dye studies (Xu et al. 2007; for a comprehensive review, see Wu et al. 2008). Even for different wave-front shapes, such as spiral waves (Huang et al. 2004), the circular shape is a reasonable approximation on

the small spatial scale covered by our electrode array (~800 μm). Distortions of the circular shape could arise from different sources: *1*) small areas within the cortex might be activated slightly earlier or later compared with the gross traveling wave front, thereby introducing an "effective" temporal jitter; and *2*) the realignment algorithm used in our study might introduce a temporal shift error, when signals superimposed by noise are presented. However, wave-front fitting (*Eq. 3*) performed well on jittered surrogate latencies, retrieving the direction reliably for normally distributed temporal jitters up to a standard deviation of ~20 ms, which is clearly more than we expect to be possibly introduced by the noise sensitivity of the realignment algorithm (Nawrot et al. 2003). In a certain fraction (~5% on average) of all transitions, we observed an unrealistically high velocity (>100 μm/ms), which might either be attributable to effective temporal jitter (e.g., the cortex activating quasisynchronously) or be introduced by a combination of temporal shift errors. Removal of these transitions did not change the results presented here. One additional concern during experiments was that the intracellular electrode itself, or tissue damage incurred by it, might be the source of state transitions. However, as in most experiments, the preferred direction did not point toward the intracellular electrode (and nor to any of the extracellular electrodes), we are confident that the observed propagating waves originated in the neuronal network itself and not at a location of an electrode or tissue injured by it. It would, however, be interesting to see whether wave propagation changes in a chronic recording with implanted electrodes.

The use of an intracellular electrode might not be feasible in other experimental preparations, particularly if the number of extracellular electrodes is increased. We therefore repeated our analysis of temporal shifts of activity within windows centered around state transitions in one extracellular electrode. This modified approach yielded the same results (data not shown), showing that our analysis is feasible also with multielectrode arrays without intracellular measurement.

An additional parameter that allows validation of our results with respect to previous findings from other groups is the wave-propagation velocity. Experimental observations revealed velocities over a range of 2–30 μm/ms (Reig et al. 2010; Ferezou et al. 2006); our findings are in the upper half of this range. Propagation velocities predicted by computational models are somewhat lower (3–8 μm/ms; Compte et al. 2003) but markedly increased when inhibition in the model was blocked (20–50 μm/ms; Compte et al. 2003). The contributions of excitatory and inhibitory neurons could not be identified in our study, as we did not sort single units from the extracellularly recorded MUA.

Waves have been reported to transcend functional borders within the cortex (Takagaki et al. 2008). However, a recent study (Xu et al. 2007) showed a more complex behavior at area borders between primary and secondary visual cortices, including compression and reflection of waves. Reflection at a nearby area border would, in our experiments, have resulted in a bimodal direction distribution, which we never observed. However, because of methodological constraints, we excluded DU transitions following very short down-states and thus might have systematically ignored reflections at area borders close to our electrode array. In any case, it remains to be demonstrated in how far our results are transferable to other brain areas as, for instance, the visual cortex described in Xu et al. (2007), and whether reflected waves could be detected if we place our electrode array over the border between two areas. A serious limitation with respect to such analysis is, however, the low number and density of electrodes that have been available for the reconstruction of the traveling waves. Obviously, it is impossible to differentiate between circular waves and more complex patterns, which might impose the same latency distributions, with only seven electrodes.

*Functional implications.* The occurrence of spontaneous slow oscillations has been demonstrated in a large variety of preparations, ranging from organotypical (Johnson and Buonomano 2007) and acute slice preparations (Sanchez-Vives and McCormick 2000; Reig et al. 2010) over deafferented cortical slabs (Timofeev et al. 2000) to experiments in the intact cortex (Steriade et al. 1993a; 1993b; 1993c; Contreras and Steriade 1995; Léger et al. 2005; Kerr et al. 2005; Waters and Helmchen 2006; Saleem et al. 2010). Additionally, in vivo experiments have been performed under a variety of conditions, particularly with respect to anesthesia. Here, the usage of ketamine/xylazine was shown to generate oscillating behavior similar to slow-wave sleep observed in sleeping animals (Sharma et al. 2010; Fontanini et al. 2003).

The function of slow oscillations and associated traveling waves has thus far remained elusive. It has been proposed that these effects play a key role in memory consolidation (Wilson and McNaughton 1994; Sejnowski and Destexhe 2000; Hoffman et al. 2007; Landsness et al. 2009), with specific activity patterns being replayed during up-states (Luczak et al. 2007; but see also Kerr et al. 2005) and a stronger activation in cortical regions that have been extensively used during wake periods (e.g., Huber et al. 2008). This view might be consistent with our finding that cortical subregions were activated in the same spatiotemporal order over many consecutive state transitions, thereby potentially introducing a high number of pattern repetitions. It is, however, difficult to judge in how far the patterns characterized in our study are stereotypical down to the level of synapses. For a validation of this issue, experiments with paired recordings in the intact animal would be the ultimate test, an experimental technique that is not available to date. Another, more tractable issue concerns the question in how far our results may be biased by the anesthetic we used. Future experiments in unanesthetized, sleeping animals could show, whether traveling waves during slow-wave sleep exhibit the same stereotypical behavior as observed here under ketamine/xylazine anesthesia. We expect a similar behavior under these two conditions, as a certain degree of stereotypical behavior has been shown in humans (Massimini et al. 2004). However, an interesting extension to the experiments we performed for this study would be *1*) to track changes in wave-propagation parameters over several sleep cycles within the same animal and *2*) to compare these results to those from animals having spent time in an enriched environment, as this might enforce consolidation during sleep of newly learned patterns, particularly in motor and sensory areas.

## GRANTS

This project received funding from the German Federal Ministry of Education and Research (BMBF grants 01GQ0413 to BCCN Berlin and 01GQ0420 to BCCN Freiburg), from the European Union (EU Grant 15879, FACETS), and from the German Research Council (DFG-SFB 780).

## DISCLOSURES

No conflicts of interest, financial or otherwise, are declared by the authors.

## REFERENCES


**Batschelet E.** *Circular Statistics in Biology (Mathematics in Biology)*. London, UK: Academic Press, 1981.

**Bazhenov M, Timofeev I, Steriade M, Sejnowski TJ.** Model of thalamocortical slow-wave sleep oscillations and transitions to activated states. *J Neurosci* 22: 8691–8704, 2002.

**Blethyn KL, Hughes SW, Tóth TI, Cope DW, Crunelli V.** Neuronal basis of the slow (<1 Hz) oscillation in neurons of the nucleus reticularis thalami in vitro. *J Neurosci* 26: 2474–2486, 2006.

**Chauvette S, Volgushev M, Timofeev I.** Origin of active states in local neocortical networks during slow sleep oscillation. *Cereb Cortex* 20: 2660–2674, 2010.

**Compte A, Sanchez-Vives MV, McCormick DA, Wang XJ.** Cellular and network mechanisms of slow oscillatory activity (<1 Hz) and wave propagations in a cortical network model. *J Neurophysiol* 89: 2707–2725, 2003.

**Contreras D, Steriade M.** Cellular basis of EEG slow rhythms: a study of dynamic corticothalamic relationships. *J Neurosci* 15: 604–622, 1995.

**Crochet S, Chauvette S, Boucetta S, Timofeev I.** Modulation of synaptic transmission in neocortex by network activities. *Eur J Neurosci* 21: 1030–1044, 2005.

**Crunelli V, Hughes SW.** The slow (<1 Hz) rhythm of non-REM sleep: a dialogue between three cardinal oscillators. *Nat Neurosci* 13: 9–17, 2010.

**Csercsa R, Dombovári B, Fabó D, Wittner L, Eross L, Entz L, Sólyom A, Rásonyi G, Szucs A, Kelemen A, Jakus R, Juhos V, Grand L, Magony A, Halász P, Freund TF, Maglóczky Z, Cash SS, Papp L, Karmos G, Halgren E, Ulbert I.** Laminar analysis of slow wave activity in humans. *Brain* 133: 2814–2829, 2010.

**Ermentrout GB, Kleinfeld D.** Traveling electrical waves in cortex: Insights from phase dynamics and speculation on a computational role. *Neuron* 29: 33–44, 2001.

**Ferezou I, Bolea S, Petersen CC.** Visualizing the cortical representation of whisker touch: voltage-sensitive dye imaging in freely moving mice. *Neuron* 50: 617–629, 2006.

**Fontanini A, Spano PF, Bower JM.** Ketamine-xylazine-induced slow (<1.5 Hz) oscillations in the rat piriform (olfactory) cortex are functionally correlated with respiration. *J Neurosci* 23: 7993–8001, 2003.

**Gabbott PL, Stewart MG.** Distribution of neurons and glia in the visual cortex (area 17) of the adult albino rat: a quantitative description. *Neuroscience* 21: 833–845, 1987.

**Hoffman KL, Battaglia FP, Harris K, MacLean JN, Marshall L, Mehta MR.** The upshot of up states in the neocortex: from slow oscillations to memory formation. *J Neurosci* 27: 11838–11841, 2007.

**Huber R, Määttä S, Esser SK, Sarasso S, Ferrarelli F, Watson A, Ferreri F, Peterson MJ, Tononi G.** Measures of cortical plasticity after transcranial paired associative stimulation predict changes in electroencephalogram slow-wave activity during subsequent sleep. *J Neurosci* 28: 7911–7918, 2008.

**Huang X, Troy WC, Yang Q, Ma H, Laing CR, Schiff SJ, Wu JY.** Spiral waves in disinhibited mammalian neocortex. *J Neurosci* 24: 9897–9902, 2004.

**Hughes SW, Cope DW, Blethyn KL, Crunelli V.** Cellular mechanism of the slow (<1 Hz) oscillation in thalamocortical neurons in vitro. *Neuron* 33: 947–958, 2002.

**Johnson HA, Buonomano DV.** Development and plasticity of spontaneous activity and up states in cortical organotypical slices. *J Neurosci* 27: 5915–5925, 2007.

**Kang S, Kitano K, Fukai T.** Structure of spontaneous UP and DOWN transitions self-organizing in a cortical network model. *PLoS Comput Biol* 4: e1000022, 2008.

**Katz LC, Shatz CJ.** Synaptic activity and the construction of cortical circuits. *Science* 274: 1133–1138, 1996.

**Kerr JN, Greenberg D, Helmchen F.** Imaging input and output of neocortical networks in vivo. *Proc Natl Acad Sci USA* 102: 14063–14068, 2005.

**Landsness EC, Crupi D, Hulse BK, Peterson MJ, Huber R, Ansari H, Coen M, Cirelli C, Benca RM, Ghilardi MF, Tononi G.** Sleep-dependent improvement in visuomotor learning: a causal role for slow waves. *Sleep* 32: 1273–1284, 2009.

**Léger JF, Stern EA, Aertsen A, Heck D.** Synaptic integration in rat frontal cortex shaped by network activity. *J Neurophysiol* 93: 281–293, 2005.

**Luczak A, Barthó P, Marguet SL, Buzsáki G, Harris KD.** Sequential structure of neocortical spontaneous activity in vivo. *Proc Natl Acad Sci USA* 104: 347–352, 2007.

**Massimini M, Amzica F.** Extracellular calcium fluctuations and intracellular potentials in the cortex during the slow sleep oscillation. *J Neurophysiol* 85: 1346–1350, 2001.

**Massimini M, Huber R, Ferrarelli F, Hill S, Tononi G.** The sleep slow oscillation as a traveling wave. *J Neurosci* 24: 6862–6870, 2004.

**Momose-Sato Y, Sato K, Kinoshita M.** Spontaneous depolarization waves of multiple origins in the embryonic rat CNS. *Eur J Neurosci* 25: 929–944, 2007.

**Nawrot MP, Aertsen A, Rotter S.** Elimination of response latency variability in neuronal spike trains. *Biol Cybern* 88: 321–334, 2003.

**Petersen CC, Grinvald A, Sakmann B.** Spatiotemporal dynamics of sensory responses in layer 2/3 of rat barrel cortex measured in vivo by voltage-sensitive dye imaging combined with whole-cell voltage recordings and neuron reconstructions. *J Neurosci* 23: 1298–1309, 2003.

**Press WH, Teukolsky SA, Vetterling WT, Flannary BP.** *Numerical Recipes in C*: the Art of Scientific Computing, 2nd ed. New York: Cambridge University, 1992.

**Reig R, Mattia M, Compte A, Belmonte C, Sanchez-Vives MV.** Temperature modulation of slow and fast cortical rhythms. *J Neurophysiol* 103: 1253–1261, 2010.

**Riedner BA, Vyazovskiy VV, Huber R, Massimini M, Esser S, Murphy M, Tononi G.** Sleep homeostasis and cortical synchronization: III. A high-density EEG study of sleep slow waves in humans. *Sleep* 30: 1643–1657, 2007.

**Rubino D, Robbins KA, Hatsopoulos NG.** Propagating waves mediate information transfer in the motor cortex. *Nat Neurosci* 9: 1549–1557, 2006.

**Sakata S, Harris KD.** Laminar structure of spontaneous and sensory-evoked population activity in auditory cortex. *Neuron* 64: 404–418, 2009.

**Saleem AB, Chadderton P, Apergis-Schoute J, Harris KD, Schultz SR.** Methods for predicting cortical UP and DOWN states from the phase of deep layer local field potentials. *J Comput Neurosci* 29: 49–62, 2010.

**Sanchez-Vives MV, McCormick DA.** Cellular and network mechanisms of rhythmic recurrent activity in neocortex. *Nat Neurosci* 3: 1027–1034, 2000.

**Sejnowski TJ, Destexhe A.** Why do we sleep? *Brain Res* 886: 208–223, 2000.

**Sharma AV, Wolansky T, Dickson CT.** A comparison of sleeplike slow oscillations in the hippocampus under ketamine and urethane anesthesia. *J Neurophysiol* 104: 932–939, 2010.

**Stark E, Abeles M.** Predicting movement from multiunit activity. *J Neurosci* 27: 8387–8394, 2007.

**Steriade M, Contreras D, Curro Dossi R, Nunez A.** The slow (<1 Hz) oscillation in reticular thalamic and thalamocortical neurons: scenario of sleep rhythm generation in interacting thalamic and neocortical networks. *J Neurosci* 13: 3284–3299, 1993a.

**Steriade M, Nunez A, Amzica F.** A novel slow (<1 Hz) oscillation of neocortical neurons in vivo: depolarizing and hyperpolarizing components. *J Neurosci* 13: 3252–3265, 1993b.

**Steriade M, Nunez A, Amzica F.** Intracellular analysis of relations between the slow (<1 Hz) neocortical oscillation and other sleep rhythms of the electroencephalogram. *J Neurosci* 13: 3266–3283, 1993c.

**Takagaki K, Zhang C, Wu JY, Lippert MT.** Crossmodal propagation of sensory-evoked and spontaneous activity in the rat neocortex. *Neurosci Lett* 431: 191–196, 2008.

**Timofeev I, Grenier F, Bazhenov M, Sejnowski T, Steriade M.** Origin of slow cortical oscillations in deafferented cortical slabs. *Cereb Cortex* 10: 1185–1199, 2000.

**Volgushev M, Chauvette S, Mukovski M, Timofeev I.** Precise long-range synchronization of activity and silence in neocortical neurons during slow-wave sleep. *J Neurosci* 26: 5665–5672, 2006.

**Vyazovskiy VV, Faraguna U, Cirelli C, Tononi G.** Triggering slow waves during NREM sleep in the rat by intracortical electrical stimulation: Effects of sleep/wake history and background activity. *J Neurophysiol* 101: 1921–1931, 2009.

**Waters J, Helmchen F.** Background synaptic activity is sparse in neocortex. *J Neurosci* 26: 8267–8277, 2006.

**Wilson MA, McNaughton BL.** Reactivation of hippocampal ensemble memories during sleep. *Science* 265: 676–679, 1994.

**Wong RO.** Retinal waves and visual system development. *Annu Rev Neurosci* 22: 29–47, 1999.

**Wu JY, Huang X, Zhang C.** Propagating waves of activity in the neocortex: What they are, what they do. *Neuroscientist* 14: 487–502, 2008.

**Xu W, Huang X, Takagaki K, Wu JY.** Compression and reflection of visually evoked cortical waves. *Neuron* 55: 119–129, 2007.